



HAL
open science

A study of bond between steel rebar and concrete under a friction-based approach

Leon Chiriatti, Hugo Ramiro Mercado Mendoza, Komla Lolonyo Apedo,
Christophe Fond, Françoise Feugeas

► To cite this version:

Leon Chiriatti, Hugo Ramiro Mercado Mendoza, Komla Lolonyo Apedo, Christophe Fond, Françoise Feugeas. A study of bond between steel rebar and concrete under a friction-based approach. *Cement and Concrete Research*, 2019, 120, pp.132-141. 10.1016/j.cemconres.2019.03.019 . hal-03171436

HAL Id: hal-03171436

<https://hal.science/hal-03171436>

Submitted on 22 Oct 2021

HAL is a multi-disciplinary open access archive for the deposit and dissemination of scientific research documents, whether they are published or not. The documents may come from teaching and research institutions in France or abroad, or from public or private research centers.

L'archive ouverte pluridisciplinaire **HAL**, est destinée au dépôt et à la diffusion de documents scientifiques de niveau recherche, publiés ou non, émanant des établissements d'enseignement et de recherche français ou étrangers, des laboratoires publics ou privés.



Distributed under a Creative Commons Attribution - NonCommercial 4.0 International License

A study of bond between steel rebar and concrete under a friction-based approach

Léon Chiriatti, Hugo Mercado-Mendoza, Komla Lolonyo Apedo,
Christophe Fond, Françoise Feugeas

1 Abstract

2 Longitudinal (rebar-axis oriented) bond behavior between ribbed re-
3 bar and concrete is closely related to the cross-sectional confinement
4 provided by the concrete cover. Few experimental data characteriz-
5 ing the concrete cover damage induced by the rebar-concrete interac-
6 tion are available. The present work aims to expand this limited exist-
7 ing database by means of an experimental campaign that includes the
8 measurement of splitting-crack development through the concrete cover.
9 Moreover, an analytical model of the rebar-concrete bond, involving the
10 introduction of only three physically-based parameters characterizing the
11 rebar-concrete interface, is proposed. These parameters are experimen-
12 tally determined through the aforementioned experimental campaign.

13 Keywords: Bond Strength (C.), Pull-Out Strength (C.), Mechanical
14 Properties (C.), Reinforcement (D.), Concrete (E.).

15 1 Introduction

16 The mechanical response of reinforced concrete (RC) structures (crack
17 width, crack spacing, deflection, tension stiffening) is highly dependent
18 on the efficiency of the shear (i.e. bond) stress transfer evenly distributed
19 all along the rough contact surface between the reinforcing bar (rebar)
20 and the concrete. ~~The rebar-concrete interface is, by its nature, deeply~~
21 ~~embedded inside the concrete bulk. This particular location makes diffi-~~
22 ~~cult any direct observation or measurement of most of the bond-related~~
23 ~~phenomena.~~ According to the state of the art [1], the description of
24 the rebar-concrete bond is essentially based on an empirical approach.

25 However, the restricted scope of empirical correlations conflicts with the
26 actual growing diversity of concretes. Indeed, empirical relationships
27 ~~mostly depend on adjustable parameters which generally lack physical~~
28 ~~meaning and which should be calibrated for each type of concrete [2, 3].~~
29 ~~In that sense, the present work aims to introduce a more predictive~~
30 ~~model, based on a greater comprehension of the damage mechanisms~~
31 ~~induced by the rebar-concrete interaction. This approach could lead to~~
32 ~~an improvement in the design of RC structures made of conventional~~
33 ~~concrete, as well as those made of new types of concrete.~~

34 Besides the longitudinal bond stress, pioneering studies [4, 5, 6, 7, 8]
35 found that the irregular shape of ribbed rebar also led to the devel-
36 opment of a cross-sectional radial stress. The possibility that the en-
37 hanced longitudinal bond capability of ribbed rebar could be related to
38 this cross-sectional radial stress was supported by numerous experimen-
39 tal studies [8, 9, 10, 11, 12]. As a result, a relationship between the
40 longitudinal bond stress and the cross-sectional radial stress, using a
41 Mohr-Coulomb failure criterion, was suggested. Meanwhile, a kinematic
42 ~~relationship~~ between the longitudinal displacement (*i.e.* slip) of the re-
43 bar and the radial displacement of the concrete cover was proposed [13].
44 Both aforementioned limit equilibrium and kinematic assumption were
45 recently coupled [14], laying the foundation for ~~the~~ predictive model of
46 ~~the rebar-concrete bond, depending on a limited amount of physically-~~
47 ~~based parameters. that is proposed in the present work.~~

48 ~~This multidirectional approach of the rebar-concrete bond is based on an~~
49 ~~accurate description of the cross-sectional damage mechanisms induced~~
50 ~~by the rebar-concrete interaction. Indeed, even though transverse rein-~~
51 ~~forcement is used, the confining action exerted by the concrete surround-~~
52 ~~ing the rebar prevails until the complete splitting of the concrete cover is~~
53 ~~attained [14]. However, such cracking level is rarely reached under service~~
54 ~~load. This implies that, for a wide range of circumstances, the rebar-con-~~
55 ~~crete bond is mainly governed by damage phenomena developing within~~
56 ~~the concrete cover. Unlike flexural cracks, splitting-cracks induced by~~
57 ~~the rebar-concrete interaction initiate inside the concrete bulk and pro-~~
58 ~~gressively develop toward the surface of the concrete cover. However,~~

59 monitoring of the crack opening is usually performed from the surface of
60 the RC member [15, 16]. Hence, many authors [14, 17, 18] highlighted a
61 lack of experimental measurements characterizing the damage develop-
62 ment preceding the complete splitting of the concrete cover. The present
63 work aims to expand this limited existing database [19, 20, 21]. For this
64 purpose, ~~an experimental procedure that includes the measurement of~~
65 ~~the splitting crack development at the rebar-concrete interface has been~~
66 ~~developed.~~ the conventional design of the sample that is generally used
67 to perform the standard pull-out test [3, 22, 23] has been modified. This
68 novel pull-out sample (see section 4) allowed the splitting-crack develop-
69 ment at the rebar-concrete interface to be measured.

70 In addition, an analytical model of the rebar-concrete bond, involving
71 the coupling between both longitudinal and cross-sectional bond-related
72 phenomena through a friction-based approach, is proposed. On the
73 basis of Tepfers' hydraulic-pressure analogy [7] and fracture mechanics
74 considerations, this model suggests that the rebar-concrete bond could
75 be analytically described by means of the introduction of only three
76 physically-based parameters characterizing the rebar-concrete interface.
77 Within this framework, an analytical expression of the rebar-concrete in-
78 terface shear stiffness (a key parameter with regard to the cracking of RC
79 structures) has been derived. All three model parameters were exper-
80 imentally determined through a pull-out test campaign including both
81 conventional and modified (see preceding paragraph) pull-out samples.
82 The comparison between measured and predicted values of the rebar-
83 concrete interface shear stiffness allowed the analytical model, that is
84 proposed in the present work, to be validated.

85 **2 Theoretical background**

86 **2.1 Longitudinal interface behavior**

87 ~~**Bond characterization**~~

88 The pull-out test, consisting in pulling a piece of rebar out of a concrete
89 bulk, is a widespread and standard [1] technique used to characterize
90 the rebar-concrete bond performance [22, 23, 24]. Basic pull-out sample
91 (Fig. 1) comprises a single rebar whose nominal diameter is referred to

92 as d_{nom} . The rebar is concentrically embedded inside a concrete cylinder
 93 providing a constant concrete cover e_{nom} . The initial anchorage length
 94 l_{adh} designates the distance along which the contact between the ribbed
 95 rebar and the concrete is effective. The pull-out test usually includes
 96 two measurements related to the longitudinal direction (z) defined by
 97 the rebar axis (Fig. 1) [25, 26]: (i) the pull-out force F applied at one
 98 loaded end of the rebar ; (ii) the relative displacement s (slip) between
 99 the rebar opposite free end and the nearest concrete surface.

100 In the case of short anchorage length ($l_{adh} \leq 7 d_{nom}$), the elongation of
 101 the rebar remains small compared to slip [13]. Hence, as a first order
 102 approximation, The motion of the rebar can be equated to a rigid body
 103 movement. This assumption implies a nearly uniform shear stress dis-
 104 tribution all along the anchorage length. In that sense, average bond
 105 stress τ corresponds to the ratio between the pull-out force F and the
 106 cylindrical surface area of the anchorage.

107 2.1.1 Bond stress

108 The pull-out test, which consists in pulling a piece of rebar out of a
 109 concrete bulk, is a widespread and standard technique used to charac-
 110 terize the rebar-concrete bond performance [1]. According to standard
 111 approaches [3, 22, 23], the conventional bond stress τ_{nom} is defined as
 112 the ratio between the pull-out force F and the nominal area of the an-
 113 chorage (Eq. 1, where d_{nom} is the nominal diameter of the rebar and l_{adh}
 114 is the initial length of the anchorage). This definition, while appropriate
 115 in the context of comparative studies [24, 25, 26], has been adjusted, in
 116 the present work, in an attempt to characterize the physical mechanisms
 117 which develop at the rebar-concrete interface.

$$118 \quad \tau_{nom} = \frac{F}{\pi d_{nom} l_{adh}} \quad (1)$$

119 The first **adjustment** concerns the effective surface area of the rebar-
 120 concrete interface. Depending on concrete properties and rebar geome-
 121 try, experimental studies have shown that three local failure mechanisms
 122 of the rebar-concrete interface may occur (Fig. 2) [1, 27]: (i) slip along

123 the rib face (mech. 1); (ii) slip along a corner made of compacted crushed
 124 concrete formed on the rib front surface (mech. 2); (iii) shear failure of
 125 the concrete trapped between the ribs (mech. 3). that shear failure of
 126 the concrete trapped between the rebar ribs (i.e. formation of a cylin-
 127 drical crack around the rebar) may occur. In this case, shear (i.e. bond)
 128 stress transfer likely stems from the friction that develops between the
 129 two flanks of the aforementioned cylindrical crack. In the present work
 130 and according to [27], the contribution of the steel-concrete contact to
 131 this friction has been neglected in comparison with that of the relatively
 132 rough concrete-concrete contact. In practice, this assumption has been
 133 taken into account through the introduction of the parameter η (Eq. 2,
 134 where $0 \leq \eta \leq 1$).

135 Each local failure mechanism can be associated with an effective contact
 136 area. On the one hand, local failure mechanism 1 is characterized by
 137 a steel-concrete contact. On the other hand, concrete-concrete friction
 138 prevails in the case of local failure mechanisms 2 and 3. The parameter
 139 η ($0 \leq \eta \leq 1$) is introduced in order to modulate the conventional cylin-
 140 drical surface area adopted in Eq. 1 with respect to the rebar-concrete
 141 effective contact area (Fig. 2).

142 The second adjustment concerns the evolving character of the initial
 143 anchorage length l_{adh} , which constantly decreases with increasing rebar
 144 slip values s . As discussed above, bond mechanisms strongly depend on
 145 the presence of concrete trapped between the rebar ribs. Hence, during a
 146 pull-out test (i.e. rebar slip), the bond efficiency of the upper unbonded
 147 (i.e. free of concrete, Fig. 1-a) portion of the rebar, which progressively
 148 enters into the sample, is practically nullified. In the present work, this
 149 issue has been addressed by adjusting the initial anchorage length l_{adh} as
 150 a function of the rebar slip measurement s (Eq. 2). Hence, the effective
 151 bond stress τ was calculated using Eq. 2.

$$152 \quad \tau = \frac{F}{\eta \pi d_{nom} (l_{adh} - s)} \quad (2)$$

153 **2.1.2 Bond parameters**

154 Longitudinal bond behavior is commonly characterized expressing the
155 average bond stress τ as a function of the rebar-concrete slip s (Fig. 2)
156 [24, 25, 26]. Given the short anchorage length that has been adopted
157 in the present work (see section 4), two failure scenarios of the pull-out
158 sample were observed:

- 159 (i) splitting-type failure: cracking of the concrete cover surrounding
160 the rebar (curve [A] in Fig. 2) ;
- 161 (ii) pull-out failure (or partial splitting): shear failure of the rebar-
162 concrete interface layer (curve [B] in Fig. 2).

163 A typical $\tau - s$ curve shows a complex shape which is generally inter-
164 preted as the sequence of three different stages (Fig. 3) [1]. Each stage is
165 related to a specific bond mechanism taking place at the rebar-concrete
166 interface. Chemical adhesion, restricted to slip values of some microm-
167 eters, represents the ability of the interface to provide bond stress τ
168 without a significant slip s . Hence, this mechanism corresponds to the
169 relatively vertical segment of the $\tau - s$ curve. After slip initiation, me-
170chanical interlocking prevails as bond stress source until slip values s of
171 about one millimeter. This hardening phase, which corresponds to the
172 $\tau - s$ curve ascending branch, is imputed to the wedging action of the ribs
173 abutting against the surrounding concrete. Pull-out failure differs from
174 splitting-type failure in the post-peak softening behavior, attributed to
175 friction, which extends to slip values of some tens of millimeters before
176 the bond stress τ reaches a nearly constant value.

177 On a comparative purpose, the following bond parameters can be defined
178 (Fig. 2) [1]:

- 179 (i) chemical adhesion strength τ_{adh} : the upper bond stress reached by
180 the interface before noticeable slip ;
- 181 (ii) interface shear stiffness k_s : the average slope of the practically
182 linear portion of the $\tau - s$ curve beyond τ_{adh} ;

183 (iii) bond strength τ_{max} : the peak stress value reached by the interface
184 throughout the pull-out test ;

185 (iv) residual friction τ_{res} : the remaining nearly constant bond stress
186 after large slip values.

187 ~~Tensile failure of concrete (moved into position 2.2.1 and re-~~
188 ~~named “Tension softening model for concrete”)~~

189 2.2 Cross-sectional interface behavior

190 During the pull-out test, whether from the manufactured irregular rebar
191 rib shape or friction phenomena taking place between fractured concrete
192 surfaces, mechanical interlocking between rebar and concrete is known
193 to cause an inclined stress field [1, 7, 10]. Free body diagram of the rebar
194 (Fig. 8 a) shows that the pull out action F is balanced by the longitudi-
195 nal (z) components τ of the stress field acting at the rebar-concrete in-
196 terface. The cross-sectional (r, θ) radial components σ are self-balanced.
197 Free body diagram of the concrete cover (Fig. 8 b) shows that the longi-
198 tudinal (z) components τ of the stress field acting at the rebar-concrete
199 interface are balanced by the support reaction. Free body diagram of
200 a horizontal slice of the concrete cover (Fig. 8 c) shows that the cross-
201 sectional (r, θ) radial components σ of the stress field acting at the re-
202 bar-concrete interface are balanced by internal circumferential (hoop)
203 stresses that develop within the concrete cover. These hoop stresses may
204 eventually lead to radial cracking of the concrete cover all along the re-
205 bar longitudinal axis. This type of crack, which has been experimentally
206 observed [9, 10], is conventionally named splitting crack [18, 19].

207 2.2.1 Tension softening model for concrete

208 Tensile failure of concrete tends to develop in a restricted volume of the
209 material named the Fracture Process Zone (FPZ) [28, 29]. This phe-
210 nomenon is known as strain localization. The area concerned by strain
211 localization, where tensile damage concentrates, is named fracture pro-
212 cess zone (FPZ). FPZ development of conventional concrete subjected
213 to direct tension successively comprises the nucleation of flaws, diffuse
214 microcracking, coalescence of microcracks, crack bridging and aggregate

215 interlocking (Fig. 4) [29, 30, 31].

216 The successive degradation mechanisms involved in concrete tensile fail-
217 ure are conventionally modeled through a tension softening curve [28,
218 29, 30]. This curve expresses the tensile damaged-concrete stress σ_D ,
219 bridging the two flanks of the Fracture Process Zone (FPZ), as a func-
220 tion of the FPZ damage level. Different approaches were developed to
221 theoretically assess the FPZ damage level [31, 32]. The fictitious-crack
222 approach developed by Hillerborg et al. [31] is adopted in the present
223 work. According to this approach, the FPZ is modeled as a discrete
224 crack, whose width w causing a displacement leap $\Delta u = w$ concentrated
225 in a zero breadth line located at x_{fpz} along the material (Fig. 5). The
226 fictitious crack opening w accounts for all damage-related displacements
227 developing from the microscale level to the macroscale one. Thus, ten-
228 sion softening curve related to the fictitious crack model expresses the
229 tensile damaged concrete stress σ_D as a function of the fictitious crack
230 opening w (Fig. 6).

231 Numerous tension softening models, for instance bi-linear [13], power
232 [33, 34] or exponential [35], can be found in the literature [29]. How-
233 ever, the tension softening curve of a concrete Representative Volume
234 Element (RVE) is generally assumed to be bi-linear (Fig. 6). Assuming
235 a bi-linear scheme, the steep S1 decrease likely corresponds to the transi-
236 tion from microscale to macroscale damage mechanisms (coalescence of
237 microcracks, C-D in Fig. 4) and the development of macroscale damage
238 (crack bridging, D-E in Fig. 4). The relatively slow S2 decrease might be
239 associated with larger macroscale mechanisms (aggregate interlocking,
240 E-F in Fig. 4).

241 Liaw et al. [30], in a study carried out on concrete specimens subjected
242 to mode I loadings, introduced a S0 plateau where the damaged concrete
243 stress σ_D is equal to the concrete tensile strength f_{ctm} for fictitious crack
244 openings w ranging from 0 to about $10 \mu m$ (Fig. 6). This plateau likely
245 corresponds to microscale damage mechanisms (nucleation of flaws and
246 diffuse microcracking, A-B and B-C in Fig. 4). Although restrained to
247 a limited domain, this plateau provides accurate results in the descrip-
248 tion of the very beginning non-linear tensile behavior of concrete. The

249 relevance of the plateau $\sigma_D = f_{ctm}$ was confirmed by Cusatis et al. [36].
 250 In other respects, Guinea et al. [37], by means of a numerical analysis
 251 carried out on modeled concrete square prisms of different sizes subjected
 252 to three point bending, showed that peak strength of concrete members
 253 subjected to flexure is systematically reached while the extreme ten-
 254 sioned fiber of the critical cross section has only undergone a limited
 255 portion of the concrete bi-linear tension softening curve (Fig. 7). Hence,
 256 as a first order approximation, softening behavior of concrete structures
 257 up to their maximum load can be modeled assuming a yield limit crite-
 258 rion equal to the concrete tensile strength f_{ctm} (Fig. 7). This criterion
 259 is consistent with the aforementioned S0 plateau introduced by Liaw et
 260 al. (Fig. 6).

261 However, on the basis of preceding studies [36, 37, 38, 39], Regarding
 262 the pull-out sample and based on the foregoing discussion, damage of
 263 the concrete bulk surrounding the rebar was taken into account, in the
 264 present work, through a constant damaged-concrete stress σ_D equal to
 265 the tensile strength of concrete f_{ctm} (Eq. 3). Hence, given this assump-
 266 tion, determination of the fracture properties of concrete was not neces-
 267 sary. As regards the undamaged concrete, a linear behavior characterized
 268 by a Young modulus denoted as E_{cm} was adopted.

$$269 \qquad \qquad \qquad \sigma_D = f_{ctm} \qquad \qquad \qquad (3)$$

270 2.2.2 Splitting-crack distribution

271 Due to strain localization, tensile failure of concrete is always a rather
 272 discrete phenomenon [3]. Hence, a finite number n of splitting cracks can
 273 be defined.

274 During a pull-out test, the cross-sectional radial stress σ acting at the
 275 rebar-concrete interface is balanced by internal circumferential (i.e. hoop)
 276 stresses σ_θ that develop within the concrete cover (Fig. 3). These hoop
 277 stresses may eventually lead to radial cracking (i.e. splitting) of the
 278 concrete cover all along the rebar longitudinal axis. This type of crack,
 279 which has been experimentally observed [10, 11], is conventionally named

280 splitting-crack [19, 18].

281 Lura et al. [18] showed by means of finite-element modeling that these
282 splitting-cracks generally develop in preferential planes. The number
283 and orientation of the splitting planes are a function of reinforcement
284 arrangement and rib geometry. In the particular case of a single con-
285 centricly embedded rebar (Fig. 1), the number and orientation of the
286 splitting planes are intrinsic properties of the rebar. In this specific con-
287 figuration and using numerical modeling, In addition, Plizzari et al. [19]
288 highlighted that only two main splitting-cracks tend to form around
289 rebars with a non-uniform rib shape similar to the crescent-ribbed rebar
290 that has been used in the present work (Fig. 4). Recent acoustic emission
291 measurements [40] confirmed this high correlation between rib shape
292 and damage distribution in the immediate vicinity of the rebar-concrete
293 interface. In the present work, a non-uniform crescent-ribbed rebar (Fig-
294 9-b), which is similar to the rebar used by Plizzari et al. [19], was used.
295 Consequently, a number n of two splitting-cracks was assumed (Eq. 4).
296 Hence, the development of a single splitting-plane, orthogonal to the axis
297 defined by the diametrically-opposed rib tips, was expected.

$$298 \qquad \qquad \qquad n = 2 \qquad \qquad \qquad (4)$$

299 2.2.3 Hydraulic-pressure analogy

300 Hydraulic pressure analogy [7, 8], developed for both discrete [12, 34]
301 and smeared [41] crack approaches, is based on the substitution of the
302 pulled-out rebar by its mechanical effect on the surrounding concrete.
303 Thus, rebar pull-out is idealized by a uniform radial stress σ exerted on
304 the rebar-concrete interface (Fig. 10-a). This specific load condition can
305 be related to the textbook case of a cylindrical tube subjected to an in-
306 ternal pressure. This axisymmetric problem yields the development of a
307 circumferential tensile state of stress $\sigma_{\theta}(r)$ through the tube wall thick-
308 ness [42], which is analogous to the hoop stresses that develop during a
309 pull-out test (Fig. 8-e).

310 The analytical model of the rebar-concrete bond proposed in the present

311 work is based on Tepfers' double cylinder model, for which comprehen-
 312 sive mathematical developments can be found in the literature [7, 9,
 313 13, 35, 33, 41]. On the basis of this existing model, the radial stress
 314 field $\sigma_r(r)$ that develops along the concrete cover thickness (i.e. between
 315 $r = r_s$ and $r = r_c$, Fig. 3) can be determined as a function of the con-
 316 crete cover damage level within the range of 0% (undamaged concrete
 317 cover) to 100% (totally damaged concrete cover).

318 ~~Solid mechanics formulas related to an elastic thick-walled cylinder sub-~~
 319 ~~jected to an internal pressure indicate that a radially decreasing state of~~
 320 ~~stress develops within the tube wall thickness [42]. Tepfers double cylin-~~
 321 ~~der model [7, 8] deals with the radial compressive stress profile $\sigma_r(r)$ and~~
 322 ~~the circumferential tensile stress profile $\sigma_\theta(r)$ (Fig. 10-a). Concrete ten-~~
 323 ~~sile strength f_{ctm} , which is (for a conventional concrete) roughly equal~~
 324 ~~to one-tenth of its compressive strength f_{cm} [43], mainly governs failure~~
 325 ~~of concrete. As a consequence, it is assumed that damage development~~
 326 ~~starts from the rebar-concrete interface ($r = r_s$) and radially extends~~
 327 ~~through the concrete wall thickness until the damaged zone eventually~~
 328 ~~reaches the edge of the concrete cover ($r = r_c$) (Fig. 10-a).~~

329 According to section 2.2.1, the behavior of the concrete cover is assumed
 330 elastic until its maximum circumferential tensile stress $\sigma_\theta(r_s)$, which
 331 is located at the rebar-concrete interface coordinate $r = r_s$, reaches
 332 the concrete tensile strength f_{ctm} . Beyond this limit, damage initiates.
 333 Damage development is then modeled by dividing the concrete cover into
 334 two rings (Fig. 3-a):

- 335 (i) a damaged inner ring ($r_s \leq r \leq r_{cr}$) governed by fracture mechanics
- 336 ;
- 337 (ii) an elastic outer ring ($r_{cr} \leq r \leq r_c$) governed by solid mechanics.

338 The boundary between these two rings is identified by the radius r_{cr} ($r_s \leq$
 339 $r_{cr} \leq r_c$), which corresponds to the location where the hoop stress
 340 $\sigma_\theta(r_{cr})$ is equal to the concrete tensile strength f_{ctm} . ~~This boundary con-~~
 341 ~~dition allows the calculation of the radial stress $\sigma_r(r_{cr})$ (Eq. 5) [12] act-~~
 342 ~~ing at the junction between the elastic outer ring and the damaged inner~~

343 ring (Fig. 10 a). Thus, the elastic outer ring can be replaced by its cor-
 344 responding confinement stress $\sigma_r(r_{cr})$. Hence, the mechanical response
 345 of the whole concrete cover can be modeled by means of a free body di-
 346 agram of the damaged inner ring (Fig. 10 b). An arbitrary sector of the
 347 damaged inner ring, defined by a given lower radius r_0 ($r_s \leq r_0 \leq r_{cr}$)
 348 and the upper radius r_{cr} , is then subjected to the following mechanical
 349 actions: (i) the radial stress $\sigma_r(r_0)$ acting along the inner circumference
 350 of the damaged concrete cover portion ; (ii) the circumferential (hoop)
 351 stress $\sigma_\theta(r^*)$ distributed within the range $r_0 \leq r^* \leq r_{cr}$; (iii) the outer
 352 radial stress $\sigma_r(r_{cr})$, due to the confinement provided by the elastic outer
 353 ring.

$$354 \quad \sigma_r(r_{cr}) = \gamma_{cr} f_{ctm} \quad \text{with} \quad \gamma_{cr} = \frac{r_c^2 - r_{cr}^2}{r_c^2 + r_{cr}^2}$$

355 Within this framework, Eq. 5 [13], can be derived from the equilibrium
 356 conditions of an arbitrary sector of the damaged inner ring, defined by
 357 a given lower radius r_0 ($r_s \leq r_0 \leq r_{cr}$) and the upper radius r_{cr} . giving
 358 the radial stress $\sigma_r(r_0)$ acting at an arbitrary coordinate r_0 along the
 359 thickness of the damaged inner ring (Fig. 3-b), can be derived.

$$360 \quad \frac{\sigma_r(r_0)}{f_{ctm}} = \frac{r_{cr}}{r_0} \gamma_{cr} + \frac{1}{r_0} \int_{r_0}^{r_{cr}} \frac{\sigma_\theta(r^*)}{f_{ctm}} dr^* \quad \text{with} \quad \gamma_{cr} = \frac{r_c^2 - r_{cr}^2}{r_c^2 + r_{cr}^2} \quad (5)$$

361 On the one hand, the inner radial stress $\sigma_r(r_0)$ depends on the damaged-
 362 concrete hoop stress profile $\sigma_\theta(r^*)$ which varies along r^* (Eq. 6). On the
 363 other hand, the damaged concrete stress σ_D can actually be correlated
 364 with Hilleborg's FPZ fictitious crack width w (Fig. 6). Accordingly In
 365 other respects, a linear relationship (Eq. 6) [13, 33] between the radial
 366 coordinate r^* (Fig. 3-b) and Hillerborg's fictitious-crack width w can
 367 also be stated.

$$368 \quad w(r^*) = \frac{2\pi}{n} \frac{f_{ctm}}{E_{cm}} (r_{cr} - r^*) \quad (6)$$

369 3 Analytical modeling

370 3.1 Radial stress equation

371 The general equations Eq. 5 and Eq. 6 taken from the literature can be
372 rewritten considering both Eq. 3 and Eq. 4 proposed in the present work,
373 and estimated in the particular case where $r_0 = r_s$, which corresponds to
374 the rebar-concrete interface coordinate. ~~Since concrete-concrete contact~~
375 ~~is found only on a fraction of the rebar-concrete interface, the parameter~~
376 ~~η , previously used to determine the effective bond stress τ (Eq. 2), was~~
377 ~~also used here. As discussed in section 2.2.1, the effective surface area~~
378 ~~of the rebar-concrete interface is taken into account through the use of~~
379 ~~the parameter η .~~ Accordingly, the radial stress σ and the FPZ opening
380 w_{fpz} , both related to the rebar-concrete interface, are given by Eq. 7
381 and Eq. 8, respectively.

382 In terms of FPZ opening, the domain of the present analytical description
383 ranges from $w_{fpz} = 0$ ($r_{cr} = r_s$, i.e. 100% elastic concrete cover) to the
384 FPZ opening corresponding to the maximum damage depth $w_{fpz} = w_{fpz}^{pl}$
385 ($r_{cr} = r_c$, i.e. 0% elastic concrete cover). This upper bound is given by
386 Eq. 9.

$$387 \quad \frac{\sigma}{f_{ctm}} = \frac{1}{\eta} \left[\frac{r_{cr}}{r_s} (\gamma_{cr} + 1) - 1 \right] \quad (7)$$

$$388 \quad w_{fpz} = \pi \frac{f_{ctm}}{E_{cm}} (r_{cr} - r_s) \quad (8)$$

$$389 \quad w_{fpz}^{pl} = \pi \frac{f_{ctm}}{E_{cm}} (r_c - r_s) \quad (9)$$

390 It can be noticed from Eq. 8 that the evolution of the radial stress acting
391 at the rebar-concrete interface σ only depends on the FPZ tip location
392 r_{cr} . Consequently, Eq. 9 appears unnecessary for determining σ . How-
393 ever the relevance of Eq. 9 comes from experimental concerns. Indeed,
394 during a pull-out test, development of the FPZ through the concrete
395 cover essentially corresponds to microscale damage phenomena such as

396 nucleation of flaws and spreading of microcracks (section 2.2). Hence,
 397 accurate experimental monitoring of the FPZ tip location r_{cr} appears
 398 difficult. However, the measurement of the FPZ opening at the rebar-
 399 concrete interface w_{fpz} , even in case of micrometric displacement, is
 400 feasible.

401 The combination of Eq. 7 and Eq. 8 leads to an analytical relation-
 402 ship (Eq. 10) between the FPZ opening w_{fpz} and the radial stress σ ,
 403 both related to the rebar-concrete interface. It can be noticed that Eq.
 404 10, established in the present work, is based on a limited number of
 405 physical and geometrical parameters, directly accessible or measurable
 406 in laboratory conditions.

$$\begin{aligned}
 407 \quad \frac{\sigma(w_{fpz})}{f_{ctm}} &= \frac{\Sigma}{\eta} \quad \text{with:} \\
 408 \quad \Sigma &= \frac{-r_s w_{fpz}^2 + 2\chi(r_c^2 - r_s^2)w_{fpz} + \chi^2 r_s(r_c^2 - r_s^2)}{r_s w_{fpz}^2 + 2\chi r_s^2 w_{fpz} + \chi^2 r_s(r_c^2 + r_s^2)} \\
 409 \quad \chi &= \pi \frac{f_{ctm}}{E_{cm}} \quad (10) \\
 410
 \end{aligned}$$

411 3.2 Longitudinal/cross-sectional coupling

412 As far as rebar-concrete interaction is concerned, the global mechanical
 413 behavior of RC structures (crack width, crack spacing, deflection, ten-
 414 sion stiffening) is mainly influenced by the longitudinal bond behavior.
 415 On the one hand, the longitudinal bond behavior $\tau - s$ (Fig. 2) is mainly
 416 described on the basis of empirical knowledge. On the other hand, Eq.
 417 10 represents a physically-based model of the cross-sectional bond be-
 418 havior $\sigma - w_{fpz}$. Hence, the coupling between the parameters related to
 419 these two directions should allow the longitudinal bond behavior to be
 420 characterized from a physical point of view.

421 3.2.1 Mohr-Coulomb failure criterion

422 The radial stress σ exerted perpendicularly to the rebar-concrete in-
 423 terface can be correlated to the rebar-concrete interface longitudinal
 424 shear strength τ assuming the Mohr-Coulomb failure criterion (Eq. 11)

425 [11, 13, 14, 33, 41]. The parameter μ is the coefficient of friction of the
 426 rebar-concrete interface and quantifies the increase of the shear strength
 427 τ due to the radial stress σ . The parameter c , called cohesion, reflects
 428 the ability of the rebar-concrete interface to withstand pure shear (i.e.
 429 τ when $\sigma = 0$).

$$430 \quad \tau = \mu \sigma + c \quad (11)$$

431 3.2.2 Kinematic compatibility equation

432 During a pull-out test, due to the particle arrangement in the immediate
 433 vicinity of the rebar-concrete interface, a radial displacement of the con-
 434 crete cover is associated with the longitudinal slip of the rebar. Indeed,
 435 The early study carried out by Den Uijl and Bigaj [13] on rebar-concrete
 436 bond modeling stated a linear relationship between the longitudinal slip
 437 of the rebar s and the radial displacement of the concrete cover. This
 438 assumption was successfully implemented by Lura et al. [18] in a finite-
 439 element model using a local linear kinematic relationship between two
 440 neighboring nodes of the mesh: one belonging to a steel element, the
 441 other to a concrete element. This linear kinematic compatibility condi-
 442 tion was also which was further used by Tastani and Pantazopoulou [14]
 443 in order to develop a multidirectional bond model.

444 Analogously, and assuming linear proportionality between the FPZ open-
 445 ing w_{fpz} and the aforementioned radial displacement, a coefficient ψ (Eq.
 446 12) has been defined in the present work. This coefficient can be inter-
 447 preted as the dilation rate of the rebar-concrete interface.

$$448 \quad w_{fpz} = \psi s \quad (12)$$

449 3.3 Shear stiffness equation

450 According to the definition given in section 2.1.3, the shear stiffness of
 451 the rebar-concrete interface k_s corresponds to the slope of the $\tau-s$ curve
 452 within its practically linear portion, right after chemical adhesion failure
 453 and slip initiation (Fig. 3). As a result, In mathematical terms, the shear

454 stiffness of the rebar-concrete interface $k_{s,TH}$ (section 2.1.2) is the limit
 455 of the derivative of the $\tau - s$ curve as the rebar-concrete slip s approaches
 456 zero (Eq. 13).

$$457 \quad k_{s,TH} = \lim_{s \rightarrow 0} \left\{ \frac{\partial \tau}{\partial s} \right\} \quad (13)$$

458 Eq. 14 is obtained from Eq. 13 by taking into consideration the Mohr-
 459 Coulomb failure criterion (Eq. 11). The coefficient of friction μ and the
 460 cohesion c are both assumed to be constant with respect to the slip s
 461 (see section 5.5).

$$462 \quad k_{s,TH} = \mu \lim_{s \rightarrow 0} \left\{ \frac{\partial \sigma}{\partial s} \right\} \quad (14)$$

463 Eq. 15 is then obtained from Eq. 14 by taking into consideration the
 464 kinematic compatibility between the rebar-concrete slip s and the FPZ
 465 opening w_{fpz} (Eq. 12).

$$466 \quad k_{s,TH} = \mu \lim_{s \rightarrow 0} \left\{ \frac{\partial w_{fpz}}{\partial s} \cdot \frac{\partial \sigma}{\partial w_{fpz}} \right\} \quad (15)$$

467 The solution of the first derivative $\frac{\partial w_{fpz}}{\partial s}$ is obtained from Eq. 12 and
 468 corresponds to the dilation rate ψ , which is assumed to be constant with
 469 respect to the slip s (see section 5.4). The second derivative $\frac{\partial \sigma}{\partial w_{fpz}}$ can be
 470 calculated from Eq. 10. Hence, the analytical expression of the interface
 471 shear stiffness $k_{s,TH}$ is given by Eq. 16.

$$472 \quad k_{s,TH} = \frac{4 \mu \psi \gamma_{cvr} E_{cm}}{\eta \pi d_{nom}} \quad \text{with} \quad \gamma_{cvr} = \frac{r_c^2 (r_c^2 - r_s^2)}{(r_c^2 + r_s^2)^2} \quad (16)$$

473 4 Materials and methods

474 4.1 Pull-out sample design

475 Pull-out samples tested in the present work (Fig. 1 and Fig. 5) com-
 476 prised a single rebar concentrically embedded inside a dodecagonal pris-
 477 matic concrete sample. As explained below, two unbonded areas were

478 implemented along the upper and lower embedded portions of the rebar.
479 Due to the non-uniform rib shape of the rebar used in this study, the
480 development of a single splitting-plane, perpendicular to the rib-tip axis,
481 was expected.

482 With reference to the conventional configuration of a pull-out sample
483 (Fig. 1-a), the geometry of the pull-out samples tested in the present
484 work (Fig. 1-b and Fig. 5) was adapted considering the following cri-
485 teria. On the one hand, the spreading of the stresses generated along
486 the anchorage area, into the concrete bulk surrounding the lower un-
487 bonded area, leads to a complex three-dimensional state of stress inside
488 the pull-out sample. Now, theoretical expressions stated in section 3 were
489 developed within a two-dimensional framework. On the other hand, due
490 to hoop stresses, the concrete bulks surrounding both the upper and
491 the lower unbonded rebar portions are likely to strongly restrain the
492 splitting-plane damage processes within the loaded anchorage area of
493 interest.

494 Thus, the pull-out sample formwork was fitted with two removable steel
495 windows positioned on both sides of the rib-dependent splitting-plane
496 (Fig. 1-b and Fig. 5-a). These steel windows, arranged so as to coincide
497 with the preferential splitting-plane, were used to split into two parts
498 the concrete bulks surrounding both the upper and the lower unbonded
499 rebar portions (Fig. 1-b and Fig. 5-b). In addition, these steel windows
500 allowed the effective (i.e. splitting-plane oriented) concrete cover c_{eff} to
501 be modulated, with the aim of studying the influence of its thickness on
502 the sample response.

503 This technical solution (i.e. steel windows) allowed a single formwork to
504 be used for the manufacturing of different concrete covers. However, the
505 resulting set-up could likely lead to parasitic notch effects along the outer
506 edges of the effective concrete cover. The influence of these notch effects
507 was assessed by means of an exploratory numerical simulation which
508 showed that the corresponding stress concentration remains marginal
509 until an advanced (i.e. clearly beyond the scope of the model proposed in
510 this work) damage development along the splitting-plane. Furthermore,
511 regardless of the concrete cover c_{eff} , no noticeable influence related to

512 these aforementioned notch effects has been experimentally observed in
 513 terms of failure mode of the pull-out samples (see section 5).

514 A first type of pull-out sample, casted in a formwork fitted with two re-
 515 movable steel windows, is hereafter referred to as beta-sample (Fig. 1-b
 516 and Fig. 5). A second type of pull-out sample, named hereafter refer-
 517 ence sample, was casted in a formwork without the use of steel window
 518 (Fig. 1-a). The notch machined on the steel window (Fig. 5-a) was
 519 designed to provide three different effective concrete covers c_{eff} (MAX,
 520 MED and MIN, Table 1). The concrete cover of reference samples (REF)
 521 was defined by the formwork inscribed radius (Fig. 5-a and Table 1).
 522 Pull-out samples were casted vertically so as to ensure a uniform distri-
 523 bution of the concrete around the rebar. Any traces of superficial cor-
 524 rosion were removed from the rebar surface with a metallic brush. Any
 525 contact between the rebar and the formwork oil was carefully avoided.
 526 All samples were vibrated and cured in an indoor stable environment
 527 ($T = 22 \pm 1^\circ\text{C}$, $RH = 72 \pm 5\%$) for 28 days.

designation	type	c_{eff} (mm)	quantity
MIN	beta	42	3
MED	beta	57	3
MAX	beta	72	3
REF	reference	87	3

Table 1: Pull-out sample categories.

528 The initial anchorage length l_{adh} was defined using Eq. 17 so as to
 529 take into account both the rebar RVE [22, 23] and the concrete RVE
 530 [30]. D is the maximum aggregate size and is equal to 20 mm. d_{nom}
 531 is the nominal diameter of the rebar and is equal to 12 mm. Thus, an
 532 initial anchorage length l_{adh} of 100 mm was implemented (Fig. 1-b).
 533 This anchorage length was short enough to ensure that the rebar state
 534 of stress remained within the elastic domain.

$$535 \quad l_{adh} = \max[5 d_{nom}; 5 D] \quad (17)$$

536 Standard prescriptions recommend an unbonded distance of at least five
 537 times the rebar diameter between the rebar-concrete anchorage area and

538 the support plate [22, 23]. This provision intends to preserve the anchor-
539 age area from parasitic stresses occurring in the vicinity of the contact
540 surface between the pull-out sample and the support plate. For this
541 purpose, the lower portion of the rebar was uncoupled from the concrete
542 cover using adhesive tape coating. A lower unbonded length of 105 mm,
543 which corresponds to the height of the steel window lower wing, was
544 chosen (Fig. 1-b). The two gaps between the steel window lower wing
545 and the lower unbonded portion of the rebar were filled with thin foam
546 stripes (Fig. 1-b and Fig. 5-a).

547 An upper unbonded length of 35 mm, larger than the maximum aggre-
548 gate size of 20 mm, was implemented using a foam tube (Fig. 1-b and
549 Fig. 5-a). This provision allowed any parasitic effect ensuing from phe-
550 nomena such as concrete bleeding, segregation and any disruption of the
551 granular stacking due to the levelling of the pull-out sample top surface,
552 to be avoided. The height of the steel window upper wing matched this
553 upper unbonded length. Ribs located above the anchorage area were
554 planed in accordance with criteria related to Eq. 2.

555 4.2 Concrete properties

556 The concrete of the pull-out samples was based on a Portland-composite
557 cement CEM II/A 42.5N, compliant with NF EN 197-1 [42], with a
558 water-to-cement ratio of 0.67. Aggregates were graded according to three
559 particle size cuts ranging from 0 mm to 20 mm. Concrete mix propor-
560 tions, designed to achieve a target compressive strength of 25 MPa, are
561 detailed in Table 2.

constituent	quantity ($\frac{kg}{m^3}$)
0/4 sand	780
4/10 fine gravel	267
6.3/20 gravel	820
limestone filler	45
Portland-composite cement	270
superplasticizer	1.31
effective water	180

Table 2: Concrete mix proportions.

562 Average values of the main hardened concrete mechanical properties,
563 determined 28 days after casting on the basis of at least three measure-

564 ments compliant with NF EN 12390 [43], are listed in Table 3. Direct
 565 tensile strength f_{ctm} was determined by means of indirect testing meth-
 566 ods (flexural strength and splitting tensile strength), using the corre-
 567 sponding correlations prescribed by NF EN 1992-1-1 [44].

property	symbol	unit	value
bulk density	ρ	$(\frac{kg}{m^3})$	2350 (6)
compressive strength	f_{cm}	(MPa)	27.2 (0.7)
direct tensile strength	f_{ctm}	(MPa)	2.4 (0.3)
Young modulus	E_{cm}	(GPa)	31.4 (0.6)

Table 3: Concrete mechanical properties (standard deviations in parentheses).

568 4.3 Rebar characteristics

569 A crescent-ribbed steel rebar, 12 mm in nominal diameter, was used.
 570 The geometrical characteristics of the two opposite ribbed rows, shaped
 571 along the rebar axis, are given in Fig. 4. According to supplier data, the
 572 Young modulus and the characteristic yield strength of the rebar steel
 573 were 200 GPa and 500 MPa, respectively.

574 4.4 Experimental set-up

575 A steel frame composed of two plates, 18 mm in thickness, connected
 576 with four threaded rods, 16 mm in diameter, was fastened to a 150 kN
 577 INSTRON 3384 testing machine (Fig. 6). The pull-out sample was
 578 positioned on the drilled lower support plate. The lower rebar end was
 579 fastened using the bottom immobile jaw of the testing machine. The
 580 upper moving jaw was used to induce a vertical displacement of the
 581 whole testing frame at a constant velocity of $0.5 \text{ mm} \cdot \text{min}^{-1}$. Therefore,
 582 the rebar pull-out was induced by the relative displacement between the
 583 ascending concrete bulk and the fastened rebar.

584 The pull-out force F was measured using a force sensor with an ac-
 585 curacy of 0.01 kN. Rebar-concrete slip s was measured using a RDP
 586 Electronics D5/300AGRA displacement sensor (LVDT) with a measur-
 587 ing range of $15 \text{ mm} \pm 0.5 \mu\text{m}$. Beyond this range, the rebar-concrete
 588 slip was determined using the built-in displacement monitoring device
 589 of the testing machine. The testing machine was computer-controlled
 590 using the INSTRON Bluehill2 manufacturer software.

591 According to section 2.2.2, the development of two distinct FPZs, ex-
592 panding in opposite directions from the rebar-concrete interface to the
593 edge of the concrete cover, was expected. In order to characterize this
594 damage development, splitting-plane opening w_{XP} was measured on
595 both sides of the rebar with an accuracy of $1.2 \mu m$ using two LVDTs
596 (Fig. 6). These LVDTs were positioned at a distance of 14 mm from
597 the rebar-concrete interface (the shortest distance given the dimensions
598 of the LVDT support). Two additional LVDTs, with an identical accu-
599 racy of $1.2 \mu m$, were positioned along the splitting-plane at a distance
600 of 54 mm from the rebar-concrete interface. These two external LVDTs,
601 used as a control measurement, showed results that were consistent with
602 those of the internal LVDTs. However, as the parameter w_{fpz} refers
603 to the FPZ opening at the rebar-concrete interface coordinate, only the
604 measurements obtained from the internal LVDTs (i.e. w_{XP}) were used
605 in the present work. In order to carry out a comparative analysis, this
606 splitting-plane opening measurement device composed of four LVDTs
607 was implemented on both beta and reference samples. In the specific
608 case of reference samples (i.e. in absence of steel windows), this de-
609 vice was arranged so as to coincide with the presumed splitting-plane
610 considering the orientation of the rib-tip axis.

611 5 Results and discussion

612 Due to technical problems, the pull-out tests performed on the first two
613 samples of category MAX (Table 1) were not achieved normally. There-
614 fore, the corresponding measurements were unusable and, thus, not con-
615 sidered hereafter.

616 5.1 Interface failure mechanism

617 The analysis of the rebar-concrete interfaces that have been performed
618 after the different pull-out tests (Fig. 7) showed that, in all cases, shear
619 failure of the concrete trapped between the ribs occurred. Thus, in ac-
620 cordance with the basic premise of the analytical model that is proposed
621 here, stress transfer along the rebar-concrete interface mainly took place
622 between the concrete fractured surfaces. The percentage of the rebar-
623 concrete interface providing a rough concrete-concrete contact was esti-

624 mated at 70 % using the rebar geometrical characteristics (Fig. 4). As
625 in [27], the potential contribution of the relatively smooth steel-concrete
626 contact was neglected. Hence, a coefficient $\eta = 0.7$ (Eq. 2) was assumed.

627 5.2 $\tau - s$ curves

628 For the different pull-out tests carried out in the present work (Table
629 1), Fig. 8-a shows the bond stress τ (Eq. 2) as a function of the cor-
630 responding free-end slip s , up to a slip value of 1.5 mm (pre-peak slip
631 range). The complete curves (i.e. slip values ranging from 0 to 30 mm)
632 are depicted in Fig. 8-b. As showed in Fig. 8-b, all reference samples
633 were subjected to pull-out failure. Splitting-type failure prevailed for all
634 the beta-samples (Fig. 1-b), except for MED-3 which underwent pull-
635 out failure. For each pull-out sample category (Table 1), average values
636 of the four bond parameters introduced in section 2.1.2 are gathered in
637 Table 4.

638 The experimental value of the interface shear stiffness k_s (Table 4) was
639 determined using a linear regression analysis (correlation coefficient of
640 at least 0.98) performed within the practically linear portion with slip
641 values ranging from 50 μm to 200 μm (k_s range in Fig. 8-a).

642 The experimental value of the chemical adhesion strength τ_{adh} was de-
643 termined as the bond stress level for a conventional slip value s of 5
644 μm which, according to Fig. 9, corresponds to the transition between
645 the strain domain (i.e. chemical adhesion stage) and the slip initiation.

646 The experimental values of τ_{adh} gathered in Table 4 suggest that this
647 parameter is not correlated with the concrete cover c_{eff} . Accordingly,
648 τ_{adh} appears related to physical mechanisms occurring in the immedi-
649 ate vicinity of the rebar-concrete interface. In that sense, based on [45],
650 the so-called chemical adhesion stage could plausibly result from a state
651 of stress of the concrete trapped between the ribs close to pure shear.

652 Indeed, in accordance with the experimental results obtained by Elige-
653 hausen et al. [25], the average value of the measured chemical adhesion
654 strength τ_{adh} (about 2.0 MPa in Table 4) was found to be close, although
655 rather lower, to the concrete tensile strength f_{ctm} (2.4 MPa in Table 3).
656 Moreover, as noticed by Tixier [46], due to rib arrangement, the internal

657 structure of the concrete trapped between the ribs tends to be closer to
658 that of mortar (cement paste and fine aggregates). This could explain,
659 at least partially, the difference between τ_{adh} and f_{ctm} .

660 Concerning beta-samples, the bond strength τ_{max} appeared directly cor-
661 related with the concrete cover c_{eff} (Table 4). In fact, through Eq. 10,
662 it can be noticed that as c_{eff} grows, the radial stress acting at the
663 rebar-concrete interface σ increases. This, given Eq. 11, could plausi-
664 bly explain this correlation. Conversely, it is worth noting that, despite
665 their larger concrete cover, reference samples generated the lowest bond
666 strength (Table 4). This could be ascribed to the global geometry of
667 this sample. Indeed, as mentioned in section 4.1, the concrete bulks
668 surrounding both the upper and the lower unbonded rebar portions are
669 likely to strongly restrain the FPZ development within the loaded an-
670 chorage area (i.e. r_{cr}), thus diminishing both terms of Eq. 6 contributing
671 to the value of σ . This assumption of the FPZ development restraint is
672 subsequently ascertained (see section 5.4) by the splitting plane open-
673 ing measurement. Indeed, as mentioned in section 4.1 and confirmed by
674 the splitting-plane opening measurements (see section 5.4), the concrete
675 bulks surrounding both the upper and the lower unbonded rebar por-
676 tions of reference samples tend to strongly restrain the FPZ development
677 (i.e. w_{fpz}) within the loaded anchorage area. Hence, according to Eq.
678 10, the larger concrete cover c_{eff} of reference samples was seemingly
679 counterbalanced by the lower FPZ opening w_{fpz} , resulting in a decrease
680 in σ . This, given Eq. 11, could explain the relatively low bond strength
681 τ_{max} that has been observed for reference samples.

682 The only beta-sample which underwent a pull-out failure (MED-3) showed
683 a residual bond stress τ_{res} which was higher than that obtained from
684 reference samples (Table 4). Again, considering the aforementioned dif-
685 ference in the FPZ development, this observation regarding τ_{res} can also
686 be explained by the relatively larger residual value of the splitting-plane
687 opening w_{XP} (Fig. 10-b), which involves larger σ (Eq. 10) and, thus,
688 larger τ (Eq. 11). In fact, beyond the shear strength of the rebar-con-
689 crete interface τ_{max} (i.e. through the softening portion of the $\tau-s$ curve
690 in Fig. 16 b), damage of the concrete-concrete contact (mech. 3 in Fig.

2), whose roughness is progressively reduced into powder, could lead to a diminution of its coefficient of friction μ (Eq. 11). Hence, the shear strength capability of the rebar-concrete interface is likely to progressively decrease until the τ_{res} plateau, which seemingly corresponds to a steady value of μ (i.e. rebar-concrete interface damaged at the highest level).

concrete cover	τ_{adh} (MPa)	τ_{max} (MPa)	τ_{res} (MPa)	k_s ($\frac{MPa}{mm}$)
MIN	2.0 (0.1)	15.9 (1.3)	-	47.0 (1.7)
MED	1.5 (0.1)	17.7 (0.6)	4.9	44 (11)
MAX	2.0	18.2	-	42.5
REF	2.1 (0.5)	15.0 (1.6)	3.9 (0.9)	16.4 (2.6)

Table 4: Bond parameters (standard deviations in parentheses).

5.3 Apparent cohesion

In order to analyse the rebar-concrete bond through a Mohr-Coulomb failure criterion (Eq. 11), apparent cohesion c had to be determined. Here, the term apparent is used to highlight the difference between the latter definition and the mechanical property generally attributed to thin cohesive soil like clay. Considering the foregoing discussion (τ_{adh} paragraph in section 5.2), and as far as the rebar-concrete interface is concerned, apparent cohesion seems to physically correspond to the interaction between the concrete trapped between the rebar ribs and the neighboring concrete, before any fracture due to the pure shear state of stress (i.e. within the strain domain).

Apparent cohesion c could be experimentally determined from the analysis of the characteristic $\tau - s$ curve previously introduced (section 5.2). Indeed, transition between the strain domain and the slip initiation could be clearly identified within the micrometric slip range of the characteristic $\tau - s$ curve (Fig. 9). In the end, the apparent cohesion c , related to the Mohr-Coulomb frictional approach, appears equivalent to the chemical adhesion strength τ_{adh} , defined in accordance with the historical description of rebar-concrete bond (section 2.1.2). This equivalence is

716 expressed by Eq. 18.

$$717 \quad c \equiv \tau_{adh} \quad (18)$$

718 5.4 Dilation rate

719 As specified in section 4.4, each pull-out sample was instrumented with a
720 pair of displacement sensors positioned perpendicularly to the preferen-
721 tial splitting-plane (Fig. 6). This instrumentation allowed the splitting-
722 plane opening at the rebar-concrete interface w_{XP} to be measured. Ex-
723 perimental results giving the splitting-plane opening w_{XP} as a function
724 of the rebar-concrete slip s are shown in Fig. 10-a (pre-peak slip range)
725 and Fig. 10-b (complete slip range). Also, the average values of the
726 maximal splitting-plane opening measurements $w_{XP,max}$ are gathered
727 in Table 5.

728 Concerning beta-samples, Fig. 10-a shows no clear correlation between
729 the concrete cover c_{eff} and the maximal splitting-plane opening $w_{XP,max}$.
730 Furthermore, splitting failure of the concrete cover systematically oc-
731 curred as w_{XP} reached a maximal value $w_{XP,max}$ close to roughly 17
732 μm (Table 5). **The existence of such a critical value of the splitting-**
733 **plane opening suggests that failure of the concrete cover could plausibly**
734 **be governed by a threshold effect (i.e. $w_{XP,max}$) rather than by the thick-**
735 **ness of the concrete cover c_{eff} .** In that sense, two damage phases may
736 be distinguished: a stable (quasi-static) damage growth and an unstable
737 (dynamic) crack propagation. ~~Given the description of concrete tensile~~
738 ~~failure introduced in section 2.2, stable damage growth could be related~~
739 ~~to scattered damage: nucleation of flaws and diffuse microcracking, (A-B~~
740 ~~and B-C in Fig. 4), while unstable crack propagation might indicate the~~
741 ~~coalescence of these microcracks (C-D in Fig. 4).~~ **The aforementioned**
742 **threshold effect is plausibly correlated with the concrete fracture prop-**
743 **erties such as the initial fracture energy G_f [47].** However, as the same
744 concrete was used for all the pull-out samples that have been tested
745 in the present work (i.e. comparable concrete fracture properties), this
746 suggests also a significant influence of local concrete heterogeneities.

747 The maximum FPZ opening values $w_{XP,max}$ of reference samples were
748 about 5 times lower than those of beta-samples (Table 5). This signif-
749 icant difference is likely attributable to the FPZ development restraint
750 previously discussed (τ_{max} and τ_{res} paragraphs in section 5.2). In fact,
751 Eq. 9 and Eq. 10 show that the splitting-plane opening w_{fpz} is correlated
752 to both the FPZ tip location r_{cp} and the radial stress at the rebar-con-
753 crete interface σ , respectively.

754 As showed in Fig. 10-a, a linear relationship between the splitting-plane
755 opening w_{XP} and the rebar-concrete slip s could be ascertained within
756 the pre-peak slip range. It is worth noting that, according to Eq. 19 (see
757 section 5.5), the FPZ opening w_{fpz} is obtained from the splitting-plane
758 opening w_{XP} by subtracting a constant displacement value Δw . The
759 dilation rate ψ (Eq. 12) can thus be calculated using either w_{fpz} or w_{XP} .
760 Hence, a constant dilation rate ψ (Table 5) could be determined from Fig.
761 10-a using a linear regression analysis (correlation coefficient of at least
762 0.94). For the beta-samples subjected to splitting-type failure, this linear
763 trend was verified until concrete cover failure (Fig. 10-a). In the case
764 of pull-out failure, the proportionality between s and w_{fpz} is effectively
765 valid within approximately the first half of the FPZ opening range (Fig.
766 10-a), probably ascertaining an early damage process occurring at the
767 rebar-concrete interface. According to Table 5, the dilation rate ψ seems
768 to be inversely correlated with the concrete cover c_{eff} , which may raise
769 questions about the character of the dilation rate as an intrinsic property
770 of the rebar-concrete interface.

771 As depicted in Fig. 10-b, in the case of pull-out failure, measurement
772 of the splitting-plane opening w_{XP} showed a significant closure of the
773 preferential splitting-plane within the post-peak slip range. For reference
774 samples, this closure was almost complete. Taking into account the FPZ
775 development restraint previously discussed (τ_{max} and τ_{res} paragraphs in
776 section 5.2), this closure is likely to be due to the elastic return of the un-
777 damaged (at least partially) part of the concrete cover. Correspondingly,
778 for the beta-samples, only a partial elastic return was observed (Fig. 10-
779 b). This could plausibly be ascribed to residual strains in relation to
780 their higher FPZ development ($w_{XP,max}$ in Table 5).

concrete cover	$w_{XP,max}$ (μm)	ψ ($\mu m/mm$)
MIN	16.5 (2.5)	33 (14)
MED	16.7 (1.6)	26 (4)
MAX	17.0	21
REF	3.0 (1.0)	4 (2)

Table 5: Kinematic parameters (standard deviations in parentheses).

781 5.5 Friction coefficient

782 According to Eq. 11, three parameters are necessary for determining
783 the friction coefficient μ inherent in the rebar-concrete interface, namely:
784 apparent cohesion c , bond stress τ and radial stress σ . Calculation of the
785 apparent cohesion c has been previously discussed (section 5.3). Bond
786 stress τ could be determined through both the pull-out force F and the
787 rebar-concrete slip s measurements (Eq. 2). The main difficulty stems
788 from the determination of the radial stress σ . Indeed, this parameter
789 is not explicitly correlated with any externally-controlled load, since it
790 results from the passive confining action of the concrete cover. However,
791 Eq. 10, developed in the present work, provides a theoretical relationship
792 between the radial stress σ and the FPZ opening w_{fpz} .

793 In that sense, it should be emphasized that the experimental measure-
794 ment of the splitting-plane opening w_{XP} could not be directly used in
795 Eq. 10. Indeed, as mentioned in section 5.4, the measurement of the
796 splitting-plane opening w_{XP} must include a part of undamaged-concrete
797 strain. However, according to the theoretical development introduced in
798 section 2, FPZ opening w_{fpz} only refers to the damaged-concrete dis-
799 placement (i.e. from the moment when the circumferential damage of the
800 concrete cover has been initiated at the rebar-concrete interface). Con-
801 sequently, the part of splitting-plane opening measurement related to
802 the undamaged-concrete strain, denoted as Δw , was subtracted from the
803 splitting-plane opening measurement w_{XP} for determining the damaged-
804 concrete displacement w_{fpz} (Eq. 19).

$$805 \quad w_{fpz} = w_{XP} - \Delta w \quad \text{with } \Delta w = \Delta w_1 + \Delta w_2 \quad (19)$$

806 In order to assess the undamaged-concrete displacement Δw , two terms

807 were added (Eq. 19). The first term, Δw_1 , accounts for the splitting-
808 plane opening w_{XP} related to the apparent cohesion stage (i.e. before
809 slip initiation, section 5.3). Accordingly, Δw_1 was determined as the
810 measured value of w_{XP} when the measured bond stress τ equals the ap-
811 parent cohesion c (i.e. when $\tau = c = \tau_{adh}$, Fig. 11-a). The second term,
812 Δw_2 , accounts for the splitting-plane opening w_{XP} measured between
813 the slip initiation and the moment when circumferential damage of the
814 concrete cover theoretically initiates at the rebar-concrete interface (i.e.
815 when $\sigma_{\theta}(r_s) = f_{ctm}$, section 2.2.3). Accordingly, Δw_2 was determined
816 by extending the curve derived from Eq. 10 down to $\sigma = 0$ (Fig. 11-b).
817 On this basis, a displacement value Δw of about $2 \mu m$ could be ascribed
818 to the undamaged-concrete strain.

819 The parallel evolution of the radial stress σ (obtained through Eq. 10
820 considering w_{fpz} as expressed in Eq. 19) and the bond stress τ (Eq. 2),
821 both represented as a function of rebar-concrete slip s , is illustrated in
822 Fig. 12-a (pre-peak slip range). As indicated on these diagrams, a given
823 slip value s^* could be used to determine the corresponding (σ^*, τ^*) state
824 of stress acting at the rebar-concrete interface. Fig. 12-b was obtained
825 by applying this operation throughout the pre-peak slip range.

826 Fig. 12-a indicates that the bond stress τ is systematically lower than the
827 radial stress σ . Consequently, a coefficient of friction lower than 1 was
828 ascertained. Moreover, it could be observed that both the bond stress
829 τ and the radial stress σ seem to follow the same asymptotic behavior.
830 This similarity is confirmed by the resulting linear trend observed within
831 a large portion of the curves depicted in Fig. 12-b. Accordingly, a
832 constant coefficient of friction μ (Table 6) could be determined for bond
833 stress values up to 80% of the bond strength τ_{max} using linear regression
834 analysis (correlation coefficient of at least 0.96). This result suggests
835 that, within the pre-peak slip range, virtually no damage of the concrete-
836 concrete contact that provides the rebar-concrete bond occurred. Hence,
837 according to the analytical model that is proposed in the present work,
838 the non-linear pre-peak behavior of the rebar-concrete bond (Fig. 8-a)
839 would mainly be attributed to the non-linear response of the damaged
840 splitting-plane (Eq. 10).

841 According to Table 6, a potential correlation between the coefficient of
842 friction μ and the concrete cover c_{eff} could be highlighted. However,
843 this possibility should be considered with caution given the correspond-
844 ing standard deviation. Moreover, as shown in [12], the coefficient of
845 friction μ is rather correlated with the rib geometry. Indeed, this param-
846 eter strongly determines the size of the aggregates that can potentially
847 be trapped between the ribs and, thus, the roughness of the concrete-
848 concrete contact.

concrete cover	c (MPa)	μ
MIN	2.0 (0.1)	0.42 (0.09)
MED	1.5 (0.1)	0.39 (0.03)
MAX	2.0	0.35

Table 6: Mohr-Coulomb parameters (standard deviations in parentheses).

849 5.6 Interface shear stiffness

850 Experimental determination of both the rate of dilation ψ and the coef-
851 ficient of friction μ allowed the interface shear stiffness $k_{s,TH}$ (Eq. 16),
852 established in the present work on the basis of a physical approach of
853 the damage phenomena taking place at the rebar-concrete interface, to
854 be calculated (Table 7). The comparison between the theoretical values
855 of the interface shear stiffness $k_{s,TH}$ and the corresponding experimental
856 values (k_s paragraph in section 5.2), both reported in Table 7, shows a
857 good correlation.

concrete cover	r_c (mm)	γ_{cvt}	$k_{s,TH}$ ($\frac{MPa}{mm}$)	k_s ($\frac{MPa}{mm}$)
MIN	48	0.95	63.5	47.0 (1.7)
MED	63	0.97	45.9	44.0 (11)
MAX	78	0.98	34.1	42.5

Table 7: Interface shear stiffness (standard deviations in parentheses).

858 6 Conclusion

859 The friction-based approach adopted in the present work, together with
860 considerations related to the damage of the concrete cover, allowed the
861 rebar-concrete pre-peak bond behavior to be analytically modeled. In
862 addition, an adaptation of the conventional pull-out test, congruent with
863 the cross-sectional description of the rebar-concrete bond, has been de-

864 veloped. From the experimental results discussed in the present work,
865 the following conclusions can be drawn:

- 866 (i) the use of removable steel windows demonstrated its ability to sub-
867 stantially reduce the confining action exerted by the concrete bulks
868 surrounding both the upper and the lower unbonded rebar por-
869 tions. This specific provision allowed the relationship between the
870 longitudinal bond behavior and the cross-sectional damage of the
871 concrete cover to be studied ;
- 872 (ii) the bond model developed in the present work requires the identifi-
873 cation of only three physically-based parameters characterizing the
874 rebar-concrete interface, namely: apparent cohesion, coefficient of
875 friction and rate of dilation. These physical parameters are likely
876 to be correlated with the rebar geometry and concrete mechanical
877 properties, thus, opening up new prospects for future research ;
- 878 (iii) the friction-based approach of the rebar-concrete bond proposed in
879 the present work allowed an analytical relationship between damage
880 development, bond stress and rebar-concrete slip to be established.
881 In contrast to existing empirical models, these physically-based re-
882 lationships could likely be used to develop a predictive service limit
883 state approach of the rebar-concrete bond ;
- 884 (iv) an analytical expression of the rebar-concrete interface shear stiff-
885 ness has been established and showed good correlation with the ex-
886 perimental measurements. This physically-based relationship rep-
887 represents an alternative to the existing empirical models and could
888 possibly lead to both an improvement in the description of the
889 mechanical response of RC structures (crack width, crack spacing,
890 deflection, tension stiffening) and a better understanding of the
891 bond between rebar and new types of concrete.

892 **Acknowledgment**

893 The Ministry of Higher Education, Research and Innovation of France
894 provided financial support (PhD scholarship No 2015-022) for the con-
895 duct of this research.

896 Declarations of interest: none.

897 References

- 898 [1] *Bond of reinforcement in concrete: state-of-art report, bulletin 10.*
899 fib (CEB-FIP), 2000.
- 900 [2] D. Shen, X. Shi, H. Zhang, X. Duan, and G. Jiang, “Experimental
901 study of early-age bond behavior between high strength concrete
902 and steel bars using a pull-out test,” *Constr. Build. Mater.*, vol. 113,
903 pp. 653–663, 2016.
- 904 [3] *fib Model Code for concrete structures 2010.* International Federa-
905 tion for Structural Concrete: fib (CEB-FIP), 2013.
- 906 [4] G. Rehm, *The basic principles of the bond between steel and con-*
907 *crete.* Cement and concrete association, 1961.
- 908 [5] L. A. Lutz and P. Gergely, “Mechanics of bond and slip of deformed
909 bars in concrete,” *ACI J.*, vol. 64, no. 11, pp. 711–721, 1967.
- 910 [6] Y. Goto, “Cracks formed in concrete around deformed tension
911 bars,” *ACI J.*, vol. 68, no. 4, pp. 244–251, 1971.
- 912 [7] R. Tepfers, *A theory of bond applied to tensile reinforcement splices*
913 *for deformed bars.* PhD thesis, Chalmers University of Technology,
914 Göteborg, Sweden, 1973.
- 915 [8] M. Maeda, S. Otani, and H. Aoyama, “Effect of confinement on
916 bond splitting behavior in reinforced concrete beams,” *Struct. Eng.*
917 *Int.*, vol. 5, no. 3, pp. 166–171, 1995.
- 918 [9] R. Tepfers, “Cracking of concrete cover along anchored deformed
919 reinforcing bars,” *Mag. Concrete Res.*, vol. 31, no. 106, pp. 3–12,
920 1979.
- 921 [10] L. J. Malvar, “Bond of reinforcement under controlled confine-
922 ment,” *Materials*, vol. 89, no. 6, pp. 593–601, 1992.
- 923 [11] R. Tepfers and P.-k. Olsson, “Ring test for evaluation of bond prop-
924 erties of reinforcing bars,” in *Proceedings of the international con-*
925 *ference Bond in Concrete, Riga, Latvia*, pp. 89–99, 1992.
- 926 [12] P. G. Gambarova and G. P. Rosati, “Bond and splitting in bar pull-
927 out: behavioural laws and concrete cover role,” *Mag. Concrete Res.*,
928 vol. 49, no. 179, pp. 99–110, 1997.
- 929 [13] J. A. Den Ujil and A. J. Bigaj, “A bond model for ribbed bars based

- 930 on concrete confinement,” *HERON*, vol. 41, pp. 201–226, 1996.
- 931 [14] S. P. Tastani and S. J. Pantazopoulou, “Reinforcement and concrete
932 bond: state determination along the development length,” *J. Struct.
933 Eng.*, vol. 139, no. 9, pp. 1567–1581, 2013.
- 934 [15] G. A. Plizzari, M. A. Deldossi, and S. Massimo, “Experimental
935 study on anchored bars in RC elements with transverse reinforce-
936 ment,” *Mater. Struct.*, vol. 29, no. 9, pp. 534–542, 1996.
- 937 [16] G. A. Plizzari, M. A. Deldossi, and S. Massimo, “Transverse rein-
938 forcement effects on anchored deformed bars,” *Mag. Concrete Res.*,
939 vol. 50, no. 2, pp. 161–178, 1998.
- 940 [17] E. Giuriani and G. A. Plizzari, “Interrelation of splitting and flexu-
941 ral cracks in RC beams,” *J. Struct. Eng.*, vol. 124, no. 9, pp. 1032–
942 1049, 1998.
- 943 [18] P. Lura, G. A. Plizzari, and P. Riva, “3D finite-element modelling
944 of splitting-crack propagation,” *Mag. Concrete Res.*, vol. 54, no. 6,
945 pp. 481–494, 2002.
- 946 [19] G. Plizzari, T. Klink, and V. Slowik, “Investigation into the failure
947 of concrete rings under inner pressure,” in *Proceedings of the in-
948 ternational conference FraMCoS-3, Gifu, Japan*, vol. 16, pp. 1311–
949 1320, 1998.
- 950 [20] M. Ghandehari, S. Krishnaswamy, and S. Shah, “Technique for
951 evaluating kinematics between rebar and concrete,” *J. Eng. Mech.*,
952 vol. 125, no. 2, pp. 234–241, 1999.
- 953 [21] M. Ghandehari, S. Krishnaswamy, and S. Shah, “Bond-induced lon-
954 gitudinal fracture in reinforced concrete,” *J. Appl. Mech.*, vol. 67,
955 no. 4, pp. 740–748, 2000.
- 956 [22] RILEM, *Technical recommendations for the testing and use of con-
957 structions materials, RC-6: Bond test for reinforcement steel (2.
958 Pull-out test)*. E & FN Spon, 1994.
- 959 [23] *NF EN 10080, Aciers pour l’armature du béton (steel reinforcing
960 bars for the reinforcement of concrete)*. Association Française de
961 Normalisation (AFNOR), 2005.
- 962 [24] A. P. Clark, “Comparative bond efficiency of deformed concrete
963 reinforcing bars,” *ACI J.*, vol. 43, no. 4, pp. 381–400, 1946.
- 964 [25] R. Eligehausen, E. P. Popov, and V. V. Bertero, “Local bond stress-

- 965 slip relationships of deformed bars under generalized excitations,”
966 Tech. Rep. UCB/EERC-83/23, October 1983.
- 967 [26] D. Darwin and E. K. Graham, “Effect of deformation height and
968 spacing on bond strength of reinforcing bars,” tech. rep., January
969 1993.
- 970 [27] C. Cao, T. Ren, C. Cook, and Y. Cao, “Analytical approach in op-
971 timising selection of rebar bolts in preventing rock bolting failure,”
972 *Int. J. Rock Mech. Min.*, vol. 72, pp. 16–25, 2014.
- 973 [28] Z. P. Bažant and J. Planas, *Fracture and size effect in concrete and
974 other quasibrittle materials*. CRC Press, december 1997.
- 975 [29] A. R. Murthy, G. S. Palani, and N. R. Iyer, “State-of-the-art review
976 on fracture analysis of concrete structural components,” *Sadhana-
977 Acad. P. Eng. S.*, vol. 34, no. 2, pp. 345–367, 2009.
- 978 [30] J. G. M. Van Mier, *Concrete fracture: a multiscale approach*. CRC
979 press, 2012.
- 980 [31] A. Hillerborg, M. Modéer, and P. E. Petersson, “Analysis of crack
981 formation and crack growth in concrete by means of fracture me-
982 chanics and finite elements,” *Cement Concrete Res.*, vol. 6, no. 6,
983 pp. 773–781, 1976.
- 984 [32] Z. P. Bažant and B. H. Oh, “Crack band theory for fracture of
985 concrete,” *Matériaux et Construction*, vol. 16, no. 3, pp. 155–177,
986 1983.
- 987 [33] M. Talaat and K. M. Mosalam, “On bond failure by splitting of
988 concrete cover surrounding anchored bars,” in *Proceedings of the
989 international conference FraMCoS-6, Catania, Italy*, pp. 789–797,
990 2007.
- 991 [34] G. Wardeh and E. Ghorbel, “Prediction of fracture parameters and
992 strain-softening behavior of concrete: effect of frost action,” *Mater.
993 Struct.*, vol. 48, pp. 123–138, 2015.
- 994 [35] C. V. Nielsen and N. Bićanić, “Radial fictitious cracking of thick-
995 walled cylinder due to bar pull-out,” *Mag. Concrete Res.*, vol. 54,
996 no. 3, pp. 215–221, 2002.
- 997 [36] D. D. Higgins and J. E. Bailey, “Fracture measurements on cement
998 paste,” *J. Mater. Sci.*, vol. 11, no. 11, pp. 1995–2003, 1976.
- 999 [37] B. M. Liaw, F. L. Jeang, J. J. Du, N. M. Hawkins, and A. S.

- 1000 Kobayashi, “Improved nonlinear model for concrete fracture,” *J.*
1001 *Eng. Mech.*, vol. 116, no. 2, pp. 429–445, 1990.
- 1002 [38] G. V. Guinea, M. Elices, and J. Planas, “Assessment of the tensile
1003 strength through size effect curves,” *Eng. Fract. Mech.*, vol. 65,
1004 no. 2, pp. 189–207, 2000.
- 1005 [39] G. Cusatis and E. A. Schaufert, “Cohesive crack analysis of size
1006 effect,” *Eng. Fract. Mech.*, vol. 76, no. 14, pp. 2163–2173, 2009.
- 1007 [40] L. Chiriatti, H. Hafid, H. R. Mercado-Mendoza, K. L.
1008 Apedo, C. Fond, and F. Feugeas, “Influence of recycled con-
1009 crete aggregate content on the rebar concrete bond proper-
1010 ties through pull-out tests and acoustic emission measurements,”
1011 in *Proceedings of the 20th International Conference on Con-
1012 crete Engineering and Technology, London, United Kingdom*
1013 (<https://waset.org/publications/10008669/>), pp. 692–699, 2018.
- 1014 [41] X. Wang and X. Liu, “A strain-softening model for steel–concrete
1015 bond,” *Cement Concrete Res.*, vol. 33, no. 10, pp. 1669–1673, 2003.
- 1016 [42] *NF EN 197-1, Ciment: composition, spécifications et critères de*
1017 *conformité des ciments courants (standard specification for cement).*
1018 Association Française de Normalisation (AFNOR), 2001.
- 1019 [43] *NF EN 12390, Essais pour béton durci (testing of hardened con-
1020 crete).* Association Française de Normalisation (AFNOR), 2012.
- 1021 [44] *NF EN 1992-1-1, Eurocode 2: calcul des structures en béton, règles*
1022 *générales et règles pour les bâtiments (design of concrete structures).*
1023 Comité Européen de Normalisation (CEN), 2005.
- 1024 [45] J. Perchat, *Traité de béton armé selon l’Eurocode 2.* Le Moniteur,
1025 2 ed., août 2013.
- 1026 [46] A. Tixier, *Analyse du comportement de l’interface acier-béton*
1027 *par essai push-in, mesures par fibres optiques et modélisation par*
1028 *éléments finis.* PhD thesis, Université Grenoble Alpes, France, 2013.
- 1029 [47] I. M. Nikbin, R. R. Saman, and H. Allahyari, “A new empirical
1030 formula for prediction of fracture energy of concrete based on the
1031 artificial neural network,” *Eng. Fract. Mech.*, vol. 186, pp. 466–482,
1032 2017.

Figure captions

Fig. 1: Design of the pull-out sample: a) conventional geometry, b) adapted geometry (distances in millimeters).

Fig. 2: Typical longitudinal bond behavior ($\tau - s$ curve) [1].

Fig. 3: Double cylinder model: a) model parameters, b) free-body diagram of the damaged inner ring.

Fig. 4: Rebar geometry (distances in millimeters and angles in degrees).

Fig. 5: Manufacturing of the pull-out sample: a) formwork, b) hardened beta-sample.

Fig. 6: Experimental set-up.

Fig. 7: Typical fractured beta-sample: a) splitting-plane, b) lateral view of the rebar.

Fig. 8: Experimental $\tau - s$ curves: a) pre-peak slip range, b) complete slip range.

Fig. 9: Experimental $\tau - s$ curves (micrometric slip range).

Fig. 10: Experimental FPZ opening: a) pre-peak slip range, b) complete slip range.

Fig. 11: Determination of Δw : a) apparent cohesion domain (Δw_1), b) undamaged-concrete domain (Δw_2).

Fig. 12: State of stress at the rebar-concrete interface: a) parallel evolution, b) Mohr plan.

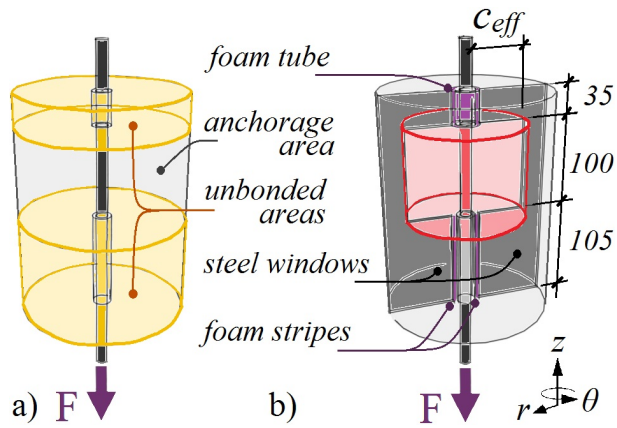


Fig. 1

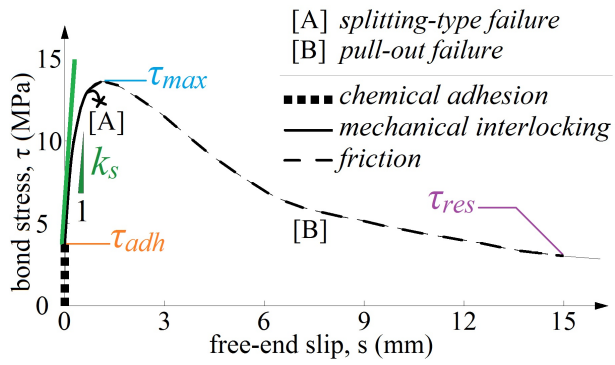


Fig. 2

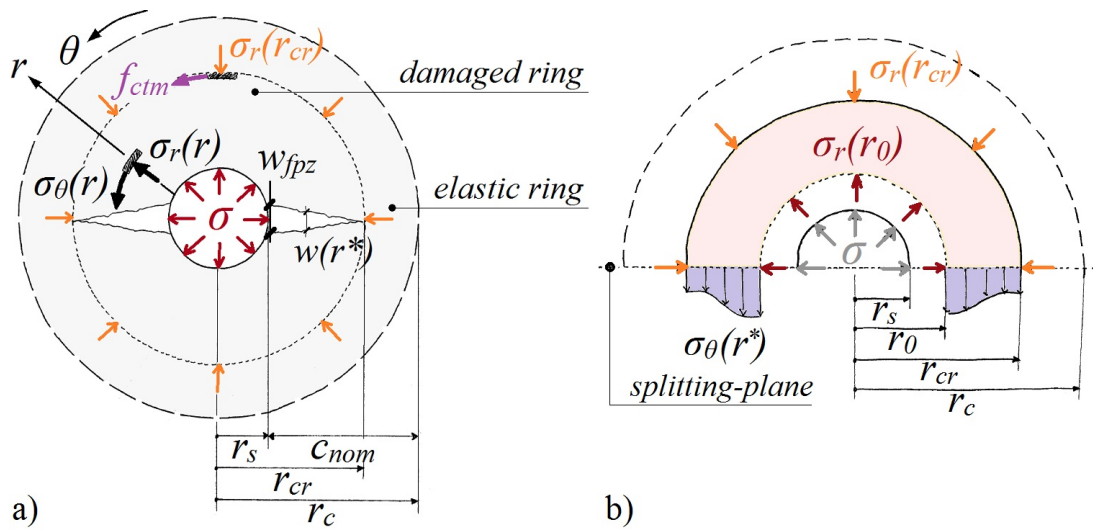


Fig. 3

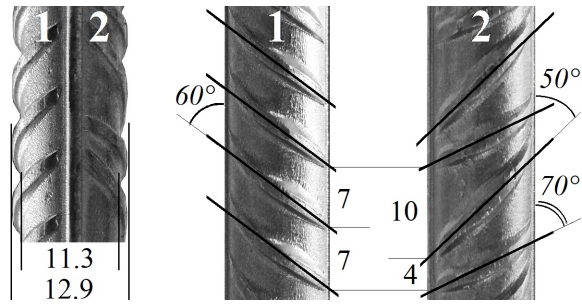


Fig. 4

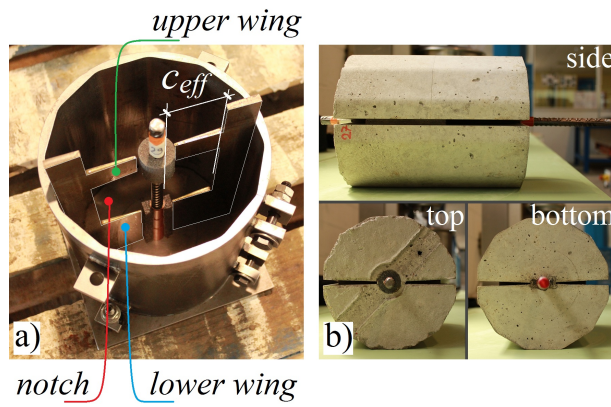


Fig. 5

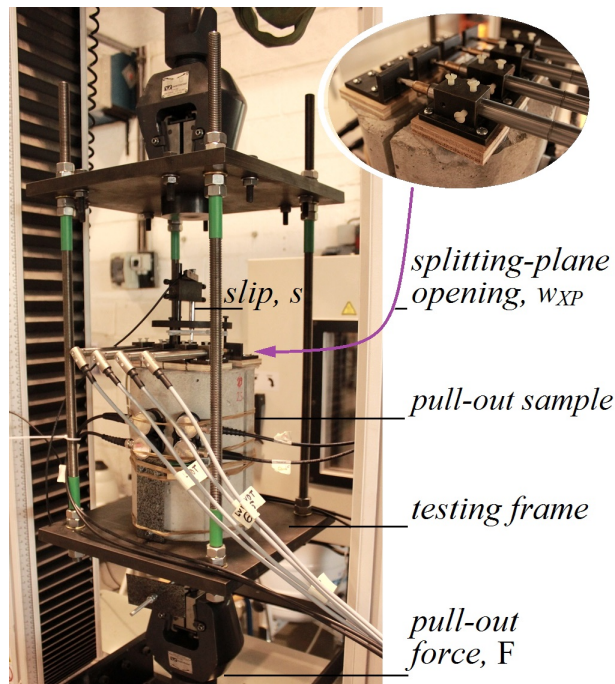


Fig. 6



Fig. 7

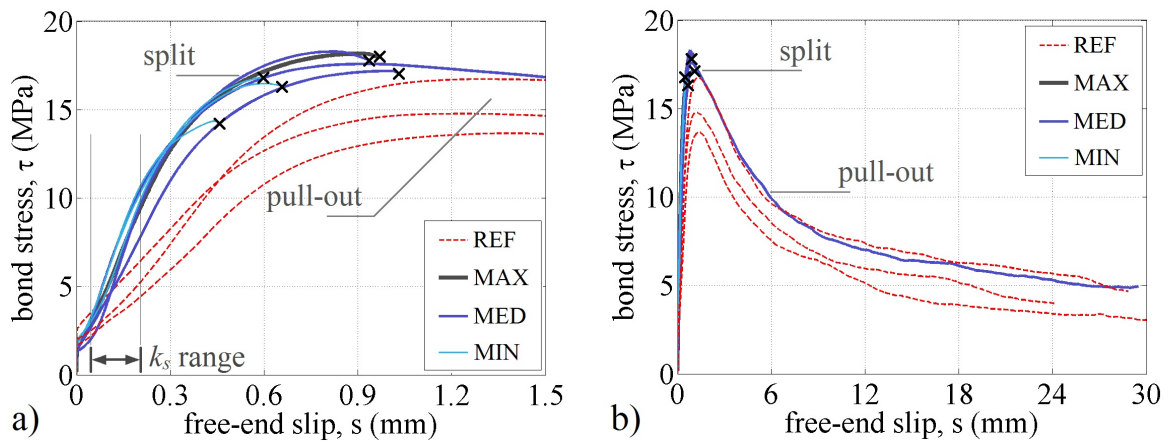


Fig. 8

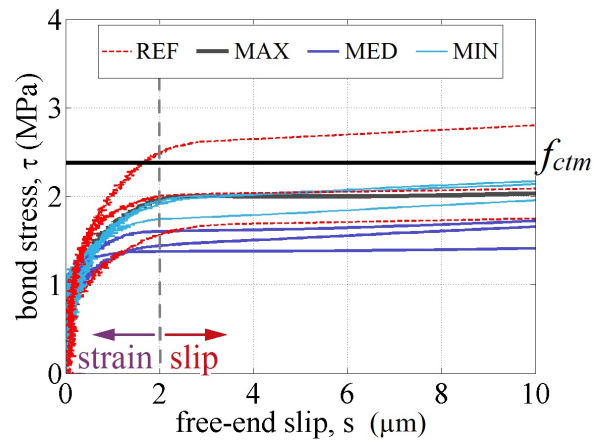


Fig. 9

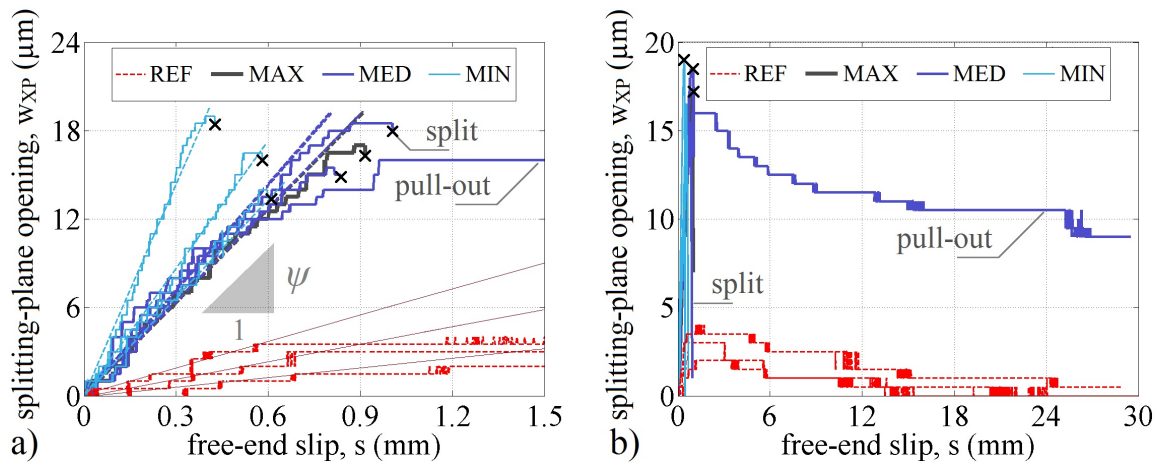


Fig. 10

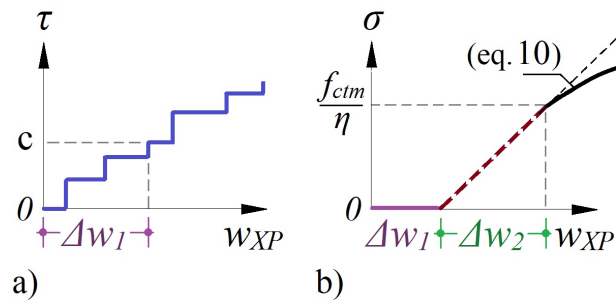


Fig. 11

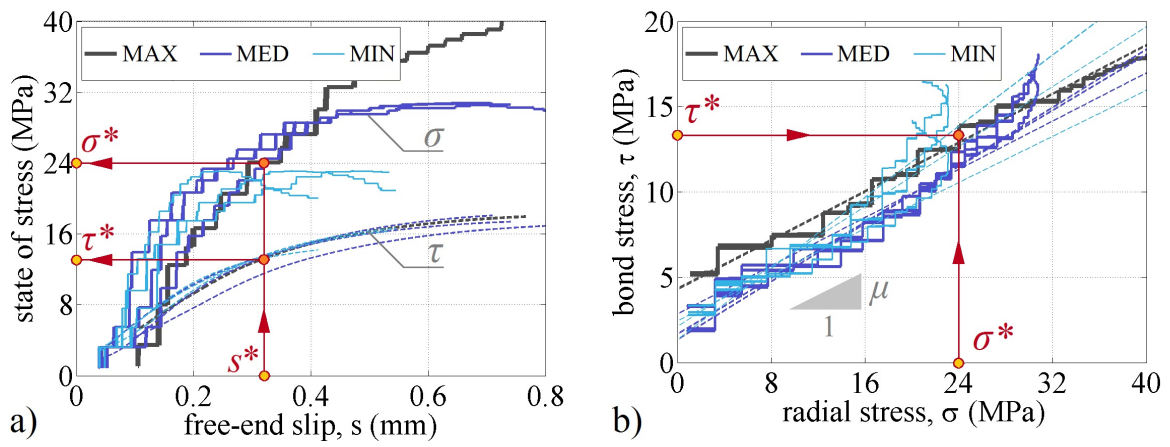


Fig. 12